Monthly Notices
of the
ROYAL ASTRONOMICAL SOCIETY

MNRAS **481,** 1631–1644 (2018)
Advance Access publication 2018 August 31

doi:10.1093/mnras/sty2368

Obscured star formation in bright $z \simeq 7$ Lyman-break galaxies

R. A. A. Bowler,[1]★ N. Bourne,[2] J. S. Dunlop,[2] R. J. McLure[2] and D. J. McLeod[2]

[1]*Astrophysics, The Denys Wilkinson Building, University of Oxford, Keble Road, Oxford OX1 3RH, UK*
[2]*Institute for Astronomy, University of Edinburgh, Royal Observatory, Edinburgh EH9 3HJ, UK*

Accepted 2018 August 25. Received 2018 August 25; in original form 2018 February 16

ABSTRACT

We present Atacama Large Millimeter/Submillimeter Array observations of the rest-frame far-infrared (FIR) dust continuum emission of six bright Lyman-break galaxies (LBGs) at $z \simeq 7$. One LBG is detected (5.2σ at peak emission), whilst the others remain individually undetected at the 3σ level. The average FIR luminosity of the sample is found to be $L_{\rm FIR} \simeq 2 \times 10^{11}\,{\rm L}_{\odot}$, corresponding to an obscured star formation rate (SFR) that is comparable to that inferred from the unobscured UV emission. In comparison to the infrared excess (IRX $= L_{\rm FIR}/L_{\rm UV}$)–β relation, our results are consistent with a Calzetti-like attenuation law (assuming a dust temperature of $T = 40$–50 K). We find a physical offset of 3 kpc between the dust continuum emission and the rest-frame UV light probed by *Hubble Space Telescope* imaging for galaxy ID65666 at $z = 7.17^{+0.09}_{-0.06}$. The offset is suggestive of an inhomogeneous dust distribution, where 75 per cent of the total star formation activity (SFR $\simeq 70\,{\rm M}_{\odot}$/yr) of the galaxy is completely obscured. Our results provide direct evidence that dust obscuration plays a key role in shaping the bright end of the observed rest-frame UV luminosity function at $z \simeq 7$, in agreement with cosmological galaxy formation simulations. The existence of a heavily obscured component of galaxy ID65666 indicates that dusty star-forming regions, or even entire galaxies, that are 'UV dark' are significant even in the $z \simeq 7$ galaxy population.

Key words: galaxies: evolution – galaxies: high-redshift.

1 INTRODUCTION

The onset of significant dust creation and obscuration in the Universe remains a key question in the study of early galaxy formation. Whilst observations and theoretical predictions indicate that dust production can be rapid (e.g. Todini & Ferrara 2001; Indebetouw et al. 2014), the relative importance of dust creation in supernovae and asymptotic giant-branch stars, grain growth, and dust destruction at high redshifts remains uncertain (e.g. Valiante et al. 2009; Michałowski 2015; Popping, Somerville & Galametz 2017). The first direct observations of the far-infrared (FIR) dust continuum at the highest redshifts were in extremely dusty star-forming systems (e.g. Riechers et al. 2013; Casey, Narayanan & Cooray 2014a) or the host galaxies of luminous quasars (e.g. Bertoldi et al. 2003; Wang et al. 2007). Now, with the sensitivity provided by the Atacama Large Millimeter/Submillimeter Array (ALMA), it is possible to measure the FIR continuum in the more 'typical' star-forming galaxy population at $z \gtrsim 6$ for the first time (Riechers et al. 2014; Capak et al. 2015; Watson et al. 2015).

Locally, the FIR emission of starburst galaxies has been found to correlate with the rest-frame UV slope (β, $F_{\lambda} \propto \lambda^{\beta}$) through the 'infrared excess–β' relation (IRX $= L_{\rm FIR}/L_{\rm UV}$; Meurer, Heckman & Calzetti 1999). Such a relationship has been found to hold up to $z \simeq 3$ (e.g. Álvarez-Márquez et al. 2016; Bourne et al. 2017; Fudamoto et al. 2017; McLure et al. 2018; Reddy et al. 2017), with several studies finding a lower normalisation that is suggestive of a steeper Small Magellanic Cloud (SMC)-like dust law (Bouwens et al. 2016; Reddy et al. 2017; although see Bourne et al. 2017; McLure et al. 2018; Koprowski et al. 2018; who found consistency with the local relation). At $z > 5$, however, the form or even existence of an IRX–β relation is uncertain. The first study to look at a sample of Lyman-break galaxies (LBGs) at $z = 5$–6 with ALMA found a deficit of FIR emission than expected from the local IRX–β relations (Capak et al. 2015; Willott et al. 2015), with several galaxies in the Capak et al. (2015) sample being undetected in the FIR continuum with ALMA despite showing red rest-frame UV colours. A stacking analysis of the ALMA Spectroscopic Survey data in the Hubble Ultra Deep Field by Bouwens et al. (2016) also found fewer detections at $z > 4$ than expected assuming the local IRX–β relation. These initial studies were interpreted as evidence for different interstellar medium properties in LBGs at high redshift. More recently, however, Koprowski et al. (2018) and McLure et al. (2018) have identified that the derived IRX–β obtained through stacking in bins of β (such as that presented in Bouwens et al. 2016) are biased to low-IRX values. Instead, Koprowski et al. (2018)

★ E-mail: rebecca.bowler@physics.ox.ac.uk

find evidence that a Calzetti-like attenuation law well describes the observations of LBGs up to $z = 4.8$.

In addition to these results, there have several direct detections of FIR continuum emission from individual LBGs at very high redshifts. The gravitationally lensed galaxy A1689-zD1 at $z = 7.5$ (Watson et al. 2015), which has a blue rest-frame UV colour ($\beta \simeq -2$) suggestive of little dust attenuation, lies significantly in excess of the local IRX–β relationship and the results of Capak et al. (2015) and Bouwens et al. (2016). Laporte et al. (2017) also claim a detection of the dust continuum in a $z = 8.38$ LBG, which has comparable FIR luminosity to A1689-zD1. The resulting picture is one of significant scatter in the IRX at a given β slope, with no compelling evidence for a correlation in the IRX–β plane at $z > 5$. Further uncertainties are introduced by the unknown dust temperature and FIR spectral energy distribution (SED) of high-redshift LBGs (Faisst et al. 2017) and the difficulty in measuring reliable β-slopes with typically faint detections in the observed near-IR (Barišić et al. 2017).

Amongst UV-selected LBGs there exists a colour–magnitude relationship until at least $z = 5$ (Rogers et al. 2014; Bouwens et al. 2014), with the most UV luminous galaxies tending to appear redder on average, with the implication that the most luminous galaxies suffer increased dust obscuration. It is therefore expected that the brightest galaxies should be dustier than the fainter galaxy population at this epoch. Indeed, at $z \simeq 5$, Cullen et al. (2017) have shown that a luminosity dependent dust correction motivated by the colour–magnitude relation can reproduce the observed rest-frame UV luminosity function (LF) in the first billion year (FiBY) simulation. In practice, many of the leading cosmological galaxy formation simulations and models currently include significant dust attenuation in order to match the observed rest-frame UV LFs at high redshifts. For example, Illustris (Genel et al. 2014), the Munich models (Henriques et al. 2015) and the analytical model of Cai et al. (2014) all apply dust obscuration of the order of $A_{\rm UV} \simeq 1$–2 mag to match the observed number densities of the brightest galaxies at $z \simeq 7$ (see fig. 13 in Bowler et al. 2015). What is required to test such models are observations that directly probe the emission from dust and hence place independent constraints on the attenuation in the rest-frame UV. In particular, observations of the brightest LBGs are a promising avenue of study as they are (1) predicted to be the dustiest galaxies from the colour–magnitude relation and (2) can be studied in detail with modest telescope time. Such observations are essential to determine the importance of dust obscuration (as opposed to other effects such as mass quenching; Peng et al. 2010) in shaping the bright end of the UV LF at the highest redshifts.

In this study, we present the results of a targeted ALMA follow-up programme to image six bright $z \simeq 7$ LBGs discovered within 1 deg^2 of overlapping deep optical/near-IR data in the Cosmological Evolution Survey (COSMOS) field (Bowler et al. 2012, 2014). We describe the new ALMA data set and auxiliary imaging in Section 2. The results are presented in Section 3, which is followed by a comparison to the IRX–β relation in Section 4. A discussion of the physical offset found between the observed dust and UV emission for ID65666, SED-fitting results, and implications for galaxy evolution simulations is presented in Section 5. We end with our conclusions in Section 6. We assume a cosmology with $H_0 = 70\,{\rm km s^{-1}\,Mpc^{-1}}$, $\Omega_{\rm m} = 0.3$, and $\Omega_\Lambda = 0.7$. Magnitudes throughout are presented in the AB system (Oke 1974; Oke & Gunn 1983).

Table 1. The coordinates of the six galaxies observed with ALMA. The coordinates correspond to the ground-based UltraVISTA DR3 centroid. The photometric redshift is shown in the final column. Furthermore, UVISTA-65666 has been spectroscopically confirmed at $z = 7.152$ (Hashimoto et al. 2018).

ID	RA (J2000)	Dec. (J2000)	$z_{\rm phot}$
UVISTA-65666	10:01:40.69	+01:54:52.42	$7.17^{+0.09}_{-0.06}$
UVISTA-304416	10:00:43.38	+02:37:51.73	$6.97^{+0.08}_{-0.04}$
UVISTA-238225	10:01:52.31	+02:25:42.24	$6.88^{+0.08}_{-0.08}$
UVISTA-169850	10:02:06.47	+02:13:24.19	$6.68^{+0.05}_{-0.04}$
UVISTA-304384	10:01:36.86	+02:37:49.14	$6.66^{+0.06}_{-0.05}$
UVISTA-279127	10:01:58.51	+02:33:08.58	$6.58^{+0.04}_{-0.05}$

2 DATA AND SAMPLE

The ALMA data were obtained in Cycle 3 through proposal 2015.1.00540.S (PI: R. A. A. Bowler). We observed the six brightest LBGs at $6.5 < z < 7.5$ presented in Bowler et al. (2012, 2014). The galaxies are all within the COSMOS field (Scoville et al. 2007a),[1] and were initially selected in the near-IR $YJHK_{\rm s}$ data based on the UltraVISTA[2] survey data release 2 (McCracken et al. 2012). The coordinates of the six galaxies, which defined each ALMA pointing, and their photometric redshifts are shown in Table 1. The galaxies were selected via SED fitting and are secure $z > 6.5$ objects as demonstrated by the sharp spectral break observed in the photometric data at $\simeq$1 μm (Fig. A1). The strength of the break ($z - Y > 2$ mag) observed in the sample cannot be reproduced by the common low-redshift or brown-dwarf contaminants (e.g. Ouchi et al. 2010; Bouwens et al. 2011; Bowler et al. 2012). Each target was observed for 10 min in Band 6 (centred at 233 GHz or 1.29 mm; corresponding to ∼170 μm in the rest frame). The integration time was chosen to provide limits on the ratio of FIR to UV luminosity sufficient to distinguish between the previous results at $z > 5$ from Watson et al. (2015) and Capak et al. (2015). The data were taken in a compact configuration C36-2, with a maximum baseline of 330 m, on 2016 January 25. In order to maximize continuum sensitivity, the correlator was set up in time division mode with 2 GHz bandwidth across each of four spectral windows (centred at 224, 226, 240, 242 GHz) in two polarizations. The data were reduced with the ALMA pipeline of CASA version 4.5.1. Calibration was performed by ALMA personnel using J1058+0133, J0948+0022, and Ganymede for bandpass, phase, and flux calibration, respectively. We then processed the data through the imaging pipeline, collapsing the full 8 GHz bandwidth and both polarizations into a single-continuum image of each field, initially using natural weighting of baselines to obtain the optimal root-mean-square (rms) sensitivity for point sources. Imaging was achieved using the TCLEAN task, and the data were cleaned by defining a mask for any source in the field with a peak signal-to-noise ratio (SNR) > 3 that also corresponds to a *Hubble Space Telescope* (*HST*)-detected galaxy (whether the target or serendipitous), with a clean threshold of 60 μJy ($\simeq 2 \times$ rms). The natural weighted images have a beam size of 1.1×1.4 arcsec full width at half-maximum (FWHM) and reach an average rms sensitivity of 27 μJy beam^{-1}, with small deviations of 2 μJy beam^{-1} between the different pointings. To increase the sensitivity to extended flux, we also tried imaging the targets with a 1 arcsec taper, which results in a beam size of 1.4×1.7 arcsec and rms

[1] http://cosmos.astro.caltech.edu
[2] http://ultravista.org/

sensitivity of 31 μJy beam^{-1}. As the natural weighted images have a smaller beam and better rms sensitivity, we chose to present this weighting throughout the paper, however comment on the tapered results where relevant. We measured fluxes using two complementary methods. First, fluxes were measured from the peak flux within an aperture of radius 1 arcsec from the *HST*/WFC3 centroid. The peak flux assumes that the source is unresolved in the ALMA data. For the stacks and the detected individual source, we also measured the total flux using a Gaussian fit. In the case of a non-detection at the 3σ level for the individual LBGs, we conservatively provide 2σ upper limits calculated as $f_{\rm peak} + 2 \times$ rms.

High-resolution rest-frame UV imaging of the sample is available from *HST*/Wide Field Camera 3 (WFC3) as described in Bowler et al. (2017). The imaging consists of a single orbit in the JH_{140} filter, which reaches a 5σ depth of $m_{\rm AB} = 27.0$ (0.6 arcsec diameter aperture). For this sample, the JH_{140} filter is uncontaminated by any Ly α emission, and hence provides a direct measurement of the rest-frame UV continuum at ∼1800 Å. The galaxy photometric redshifts and stellar masses were determined from SED fitting to the deep multiwavelength photometric data available over the COSMOS field. This includes *Spitzer*/IRAC data from the SPLASH (Steinhardt et al. 2014)[3] and SMUVS (Ashby et al. 2018) surveys, near-IR data from the third data release of UltraVISTA (McCracken et al. 2012) and finally optical data from Subaru/SuprimeCam (Furusawa et al. 2016) and the Hyper-SurprimeCam (HSC) Subaru Strategic Program (Aihara et al. 2017). The photometric redshift code LEPHARE was used (Arnouts et al. 1999; Ilbert et al. 2006) to perform the SED-fitting analysis. We fitted Bruzual & Charlot (2003) models, assuming an exponentially declining star formation history (SFH), a Chabrier (2003) initial mass function (IMF), and a metallicity of 1/5 $Z_\odot$. The τ parameter defining the characteristic time-scale of the SFH ranged between 50 Myr and 10 Gyr, approximating both a burst and constant SFH in the extreme cases. The minimum galaxy age was set to 10 Myr, with the maximum age set by the age of the Universe at each redshift. Dust attenuation was applied assuming a Calzetti et al. (2000) dust law. The best-fitting SED models along with the photometry for our sample is shown in Fig. A1. We measured photometry in 1.8 arcsec diameter apertures, correcting to total flux using a point source correction determined using PSFEx (Bertin 2011). Errors were obtained using local depths determined from the closest 200 empty apertures to each galaxy. *Spitzer*/IRAC data were deconfused using TPHOT following the procedure outlined in McLeod, McLure & Dunlop (2016). Further details of the ground-based images and data reduction can be found in Bowler et al. (2014).

3 RESULTS

The new ALMA data for our sample is shown in comparison to the *HST*/WFC3 JH_{140} imaging in Fig. 1. We find that one galaxy in our sample (ID65666) is clearly detected in the ALMA images, with a measured peak flux of 124 ± 24 μJy or 5.2σ significance. ID65666 is the highest-redshift galaxy we targeted, with a best-fitting photometric redshift of $z = 7.17^{+0.09}_{-0.06}$. The inclusion of new HSC data as shown in Fig. A1 results in a slightly higher (but consistent) photometric redshift than previously obtained ($z = 7.04^{+0.16}_{-0.15}$; Bowler et al. 2017). The photometric redshift we find is consistent with the tentative detection of the Ly α emission line at $z = 7.168$ for this object by Furusawa et al. (2016), and the recently the spectroscopic redshift of $z = 7.152$ derived from the FIR lines [O III] 88 μm and [C II] 158 μm by Hashimoto et al. (2018). We found a slight (10 per cent) increase in SNR for ID65666 when using the 1 arcsec tapered image, indicating that the dust emission is extended on this scale. Such an extension is comparable to the size of the rest-frame UV emission seen in Fig. 1. Using a Gaussian fit to account for this extended emission results in a total flux of 168 ± 56 μ Jy. The ALMA detection and the JH_{140} image show an offset of ≃0.6 arcsec, which we discuss further in Section 5.1. The remaining galaxies are undetected at the 3σ level. The measured fluxes and 2σ upper limits are presented in Table 2. Four of the six LBGs presented here show multiple components in the high-resolution *HST*/WFC3 imaging. In Bowler et al. (2017), we checked whether each clump was consistent with being at $z > 6.5$ using the deep *HST*/Advanced Camera for Surveys I_{814} data available in the COSMOS field (Koekemoer et al. 2007; Scoville et al. 2007b; Massey et al. 2010). This analysis confirmed that the components found

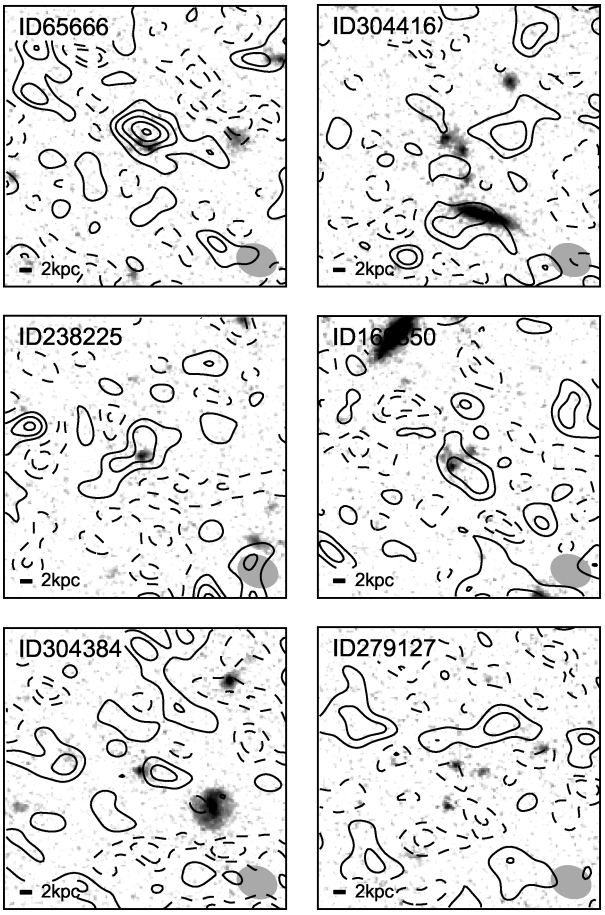

Figure 1. The six $z \simeq 7$ LBGs targeted in this study, shown in order of descending redshift from top left to lower right. The background image is the *HST*/WFC3 JH_{140} data, and the contours show the results of our ALMA 1.3 mm observations with natural weighting. The images are 10 arcsec on the side, with north to the top and east to the left. The ALMA contours are drawn at 1σ intervals (negative contours are shown as dotted lines). The beam is shown as the ellipse in the lower right-hand corner of each stamp. The grey-scale for the background *HST* image is linearly scaled from a minimum surface brightness of 26 mag arcsec^{-2} to the peak brightness of the primary target.

[3] http://splash.caltech.edu

Table 2. The observed ALMA flux and derived properties of the sample of six bright LBGs. The galaxies are ordered in descending redshift, as in Table 1. The upper part of the table shows the individual results, and the lower part shows the stacked results. The rest-frame UV slope (β; see Section 4) is presented in column 2, followed by the absolute UV magnitude and the corresponding monochromatic luminosity in columns 3 and 4. The observed 1.3 mm flux, or upper limit on the flux, is shown in column 5. For the detected object ID65666, the total flux is determined from a Gaussian fit. This is followed by the FIR luminosity derived using a modified blackbody fit assuming $T = 40$ K is shown in column 6. The ratio of the FIR to UV luminosity, IRX, is presented in column 7. Finally, in columns 8 and 9, we show the star formation rate (SFR) in the FIR and the stellar mass, respectively.

ID	β	$M_{\rm UV}$ (mag)	$L_{\rm UV}$ (10^{11} L$_\odot$)	$f_{1.3\,\rm mm}$ (μJy)	$L_{\rm FIR}$ (10^{11} L$_\odot$)	log(IRX)	SFR$_{\rm FIR}$ (M$_\odot$ yr^{-1})	log(M_*/M$_\odot$)
UVISTA-65666	$-1.85^{+0.54}_{-0.53}$	$-22.43^{+0.11}_{-0.10}$	1.98 ± 0.19	168 ± 56	3.63 ± 1.21	$0.26^{+0.17}_{-0.22}$	50 ± 17	$9.0^{+0.8}_{-0.2}$
UVISTA-304416	$-2.26^{+0.53}_{-0.53}$	$-23.16^{+0.10}_{-0.09}$	3.89 ± 0.34	<106	<2.36	<-0.22	<33	$9.6^{+0.4}_{-0.2}$
UVISTA-238225	$-2.00^{+0.59}_{-0.63}$	$-22.41^{+0.12}_{-0.12}$	1.95 ± 0.22	<139	<3.02	<0.19	<42	$9.6^{+0.4}_{-0.2}$
UVISTA-169850	$-1.80^{+0.29}_{-0.29}$	$-22.92^{+0.12}_{-0.10}$	3.12 ± 0.31	<129	<2.90	<-0.03	<40	$9.4^{+0.6}_{-0.2}$
UVISTA-304384	$-1.86^{+0.35}_{-0.36}$	$-22.40^{+0.11}_{-0.10}$	1.93 ± 0.19	<127	<2.84	<0.17	<39	$9.5^{+0.6}_{-0.2}$
UVISTA-279127	$-2.25^{+0.37}_{-0.39}$	$-22.62^{+0.18}_{-0.15}$	2.36 ± 0.36	<92	<2.00	<-0.07	<28	$9.5^{+0.6}_{-0.6}$
Full stack	$-2.00^{+0.19}_{-0.19}$	$-22.76^{+0.05}_{-0.06}$	2.69 ± 0.14	101 ± 34	2.26 ± 0.76	$-0.08^{+0.15}_{-0.20}$	31 ± 11	–
Non detections	$-2.03^{+0.20}_{-0.20}$	$-22.81^{+0.05}_{-0.06}$	2.82 ± 0.14	100 ± 50	2.23 ± 1.12	$-0.10^{+0.20}_{-0.32}$	31 ± 16	–

within 0.5 arcsec[4] were genuinely associated with the high-redshift LBG, with each clump showing a strong optical-to-near-IR colour exceeding $I_{814} - JH_{140} \gtrsim 1.5$. The probability of chance alignment of a very red, low-redshift interloper, with our high-redshift sample, is expected to be very small (<1 per cent; Bowler et al. 2017).

The calculation of the total rest-frame FIR luminosity ($L_{\rm FIR}$) from the observed single data point at 1.3 mm requires the assumption of a SED in the FIR. To provide a straightforward comparison to previous studies we calculated the $L_{\rm FIR}$ first using a simple modified blackbody (grey body) curve, of the form $f_\nu \propto \nu^\beta B_\nu(T)$, assuming an optically thin medium. We fix the exponent to $\beta = 1.6$, which is the best-fitting value from the sample of local IR luminous galaxies presented in Casey (2012). A dust temperature of $T = 40$ K was taken as our fiducial value. This is motived by the results of Coppin et al. (2015), who found a best-fitting dust temperature of $T = 37$–38 K through a stacking analysis of LBGs at $z = 3$–5 (see also Fudamoto et al. 2017; Knudsen et al. 2017; Koprowski et al. 2018). Assuming this dust temperature allows a more direct comparison to previous works from Watson et al. (2015), who assumed 40 K and to Capak et al. (2015) who used dust temperatures in the range of $T = 25$–45 K. It has been suggested that at high redshift the dust temperature could be higher than is typically found at lower redshifts (e.g. Faisst et al. 2017; Schreiber et al. 2017). Hence, we also fit the observations assuming a higher dust temperature of 50 K. We investigated the effect of allowing β to vary according to the 1σ range found at lower redshift (Casey 2012). The resulting variation in the derived FIR luminosity was found to be <10 per cent. As this additional error is small in comparison to the error on the flux, we neglect it in the following analysis. In Capak et al. (2015), an alternative parametrization of the FIR SED was used that includes an additional power-law component in the mid-IR. Using such a parametrization results in brighter FIR luminosities by a factor of 1.63 ± 0.15 (using the form and best-fitting parameters, and errors, presented by Casey 2012). Finally, we calculate $L_{\rm FIR}$ using the empirical FIR SEDs from several lower-redshift starburst galaxies: Arp220, M82, and with the average SED of submillimetre galaxies derived by Michałowski et al. (2010) and Pope et al. (2008). We account for the reduced contrast due to the higher temperature of the cosmic microwave background (CMB; $T \simeq 22$ K at $z = 7$) using the approach presented in da Cunha et al. (2013). The dust temperatures quoted above correspond to the temperature after any CMB heating has taken place. The total luminosity was calculated by integrating under the FIR SED from 8 to 1000 μm. The resulting $L_{\rm FIR}$ assuming a dust temperature of $T = 40$ K are presented in Table 2. The assumption of a higher dust temperature results in an increase in the FIR luminosity of a factor of 2. Using the range of empirical galaxy templates results in an increase of $\simeq$1 for Apr220, $\simeq$2 for M82, and $\simeq$ 0.9 and $\simeq$ 1.5 for the submillimetre templates of Michałowski et al. (2010) and Pope et al. (2008), respectively.

The detection and upper limits on the FIR luminosity that we derive exceed that found in the majority of previous ALMA detections at $z > 5$. We compare our derived UV and FIR luminosities for the sample to those from previous studies at these redshifts in Fig. 2. The detected galaxy, ID65666, shows $L_{\rm FIR} = 3.63 \pm 1.21 \times 10^{11}$ L$_\odot$ ($T = 40$ K) which is substantially brighter than 80 per cent of the sample presented by Capak et al. (2015) at $z = 5$–6 LBGs. ID65666 is over twice as luminous in the FIR than both of the $z > 7$ detections presented by Watson et al. (2015) and Laporte et al. (2017) ($L_{\rm FIR} = 6.2 \times 10^{10}$ L$_\odot$ and $L_{\rm FIR} = 7-18 \times 10^{10}$ L$_\odot$, respectively). For the other five galaxies with non-detections in the ALMA data, we derive conservative upper limits of $L_{\rm FIR} \lesssim 2-3 \times 10^{11}$ L$_\odot$ (2σ).

3.1 Stacking results

We stacked the ALMA Band 6 data to determine the average FIR luminosity for our sample. The stacks are shown in Fig. 3. The data were stacked using the UltraVISTA K_s-band centroid of each LBG. The K_s band was used in preference to the *HST* data, as it probes a longer wavelength that is more likely to be representative of the peak in stellar mass, rather than tracing only recent star formation. In reality, these coordinates are within 0.1 arcsec of the *HST*/WFC3 coordinates, and hence, this makes no difference to our conclusions. We produced two stacks, one with all six galaxies included, and one where our detected galaxy ID65666 was excluded. We find a detection at the 4σ level in the full stack ($f_{1.3\rm mm} = 46 \pm 11$ μJy beam^{-1}), and a more tentative detection with a peak at 2.9σ ($f_{1.3\rm mm} = 35 \pm 12$ μJy beam^{-1}) in the stack of the non-detections. Using the Gaussian fit results in a higher measured

[4]At separations of greater than ∼0.5 arcsec from the high-redshift target, we find lower redshift galaxies along the line of sight. In particular, the small clump between the edge-on spiral and the dual cored LBG in object ID304416 is detected in the *HST*/ACS data and is therefore not associated with the $z = 6.85$ galaxy. Furthermore, the object to the lower left of the two more widely separated components of ID279127 is also detected in the I_{814} data and is therefore also at lower redshift.

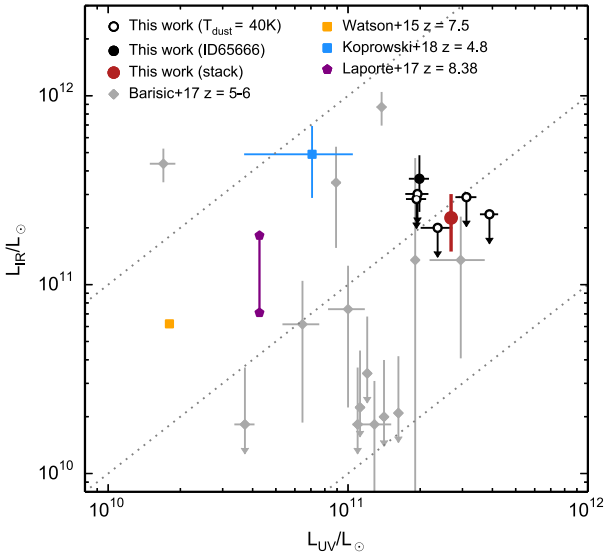

Figure 2. The rest-frame UV luminosity compared to the derived rest-frame FIR luminosity for a compilation of studies at $z \gtrsim 5$, where ALMA detections have been found. For Laporte et al. (2017), we display the range of acceptable values derived in their work. The dotted lines show the position of IRX = [1.0, 0.0, −1.0] from top to bottom to guide the eye. The LBGs that we targeted with ALMA represent the most UV luminous galaxies known at $z \simeq 7$ to date.

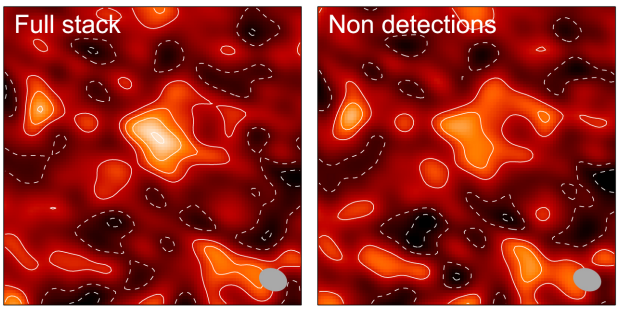

Figure 3. The results of stacking the ALMA data for our sample. The images are 15 arcsec on the side and show the Band 6 data stacked at the centroid position of the LBG in the UltraVISTA K_s-band image. The left-hand plot shows the results of stacking the full sample, whereas in the right-hand stack the detected object ID65666 has been removed. The colour scale is linear and identical in each plot. The beam is shown as the filled grey ellipse.

flux, indicating that the stacked flux is extended at the resolution of the ALMA data. This can also be seen visually in the stacks, and could be a consequence of offsets between the FIR and UV emission (Section 5.1), and/or the FIR emission being resolved in the ALMA data (as we find for ID65666). We therefore determine the average FIR luminosity of the stacks using the flux determined from the Gaussian fit, and present these results in Table 2. Reassuringly, the results for the full stack and the stack of the non-detections are very similar (although the uncertainty in the derived FIR for the non-detections stack is large), indicating that the detected galaxy does not dominate the stacked flux. The average FIR luminosity that we derive, $L_{\rm FIR} \simeq 2 \times 10^{11}\,{\rm L}_{\odot}$, is significantly brighter than the majority of the Capak et al. (2015) sample, which were measured to have $L_{\rm FIR} < 2 \times 10^{10}\,{\rm L}_{\odot}$. As the UV luminosities for our sample and this $z = 5$–6 sample are comparable, we therefore derive substantially higher IRX values than found by Capak et al. (2015). We discuss this further in reference to the IRX–β relation in Section 4.

3.2 Serendipitous detections and astrometric accuracy

The primary beam of the ALMA images has an FWHM of 26 arcsec, and since sensitivity falls off gradually with radial distance from the centre, this allows background sources to be detected serendipitously. From inspecting the ALMA data, we visually identified two bright sources likely corresponding to other galaxies within the field of view of the images for primary targets ID65666 and ID238225. In addition to a visual inspection, we blindly extracted sources from the images following a similar procedure to that of Dunlop et al. (2017). We first created an SNR map to use as the detection image: this is given by the cleaned image (before primary beam correction) divided by the measured rms in that image. Sources were identified by finding the peak SNR pixel and then fitting an elliptical Gaussian profile to this position in the primary beam-corrected image. After fitting and subtracting the model from the image, the process was repeated if the residual SNR map contained a peak >3.5. The result was 17 potential sources over the six pointings. As described in Dunlop et al. (2017), however, the noise properties of the ALMA data are such that at this significance level we expect more than half of these sources to be spurious. We therefore cross-matched the ALMA sources with sources detected at $>5\sigma$ significance in the *HST*/WFC3 JH_{140} image. The result is a sample of five robust sources from the maps, one of which is the primary target ID65666 at $z = 7.17^{+0.09}_{-0.06}$. The properties of these sources are detailed in Table 3. The ALMA Band 6 data and the *HST*/WFC3 imaging for the four additional sources are shown in Fig. 4. One of the serendipitous detections has been spectroscopically confirmed at $z = 0.8268$ as part of the zCOSMOS programme (Lilly et al. 2007). This source is also detected in the *Chandra* X-ray catalogue ('lid_38'; Civano et al. 2016). For the other sources, we quote the photometric redshifts from the COSMOS2015 catalogue (Laigle et al. 2016). Three of the sources are detected in the COSMOS Very Large Array (VLA) 3 GHz data.

The detection of these sources, and in particular an object in the same primary beam as our detected high-redshift galaxy ID65666, provides an additional test of the astrometric accuracy. The astrometry of the *HST*/WFC3 data was tied to that of the UltraVISTA DR3 images,[5] which in turn is matched to 2-Micron All-Sky Survey (Magnier et al. 2016). The expected astrometric accuracy of the two data sets is of order ∼0.1 arcsec, as this is the median offset found when matching the UltraVISTA (and hence *HST*/WFC3) data to external catalogues. Such a shift represents < 1 pixel in the ground-based imaging. We checked the astrometric accuracy of the UltraVISTA DR3 data by matching the full catalogue (covering 1.5 deg^2) to the AllWISE and COSMOS VLA catalogues, finding excellent agreement and no evidence for a systematic offset larger than 0.05 arcsec. In Table 3 we present the measured astrometric offsets found between the 1.3 mm emission and the JH_{140} centroid for the ALMA detected serendipitous sources. The JH_{140} centroid was determined by SExtractor, which calculates the barycentre or first order moment of the light profile (Bertin & Arnouts 1996). For the two faintest serendipitous sources (C3 and C4) we find offsets between the ALMA profile and the JH_{140} centroid. As is evident from the images shown in Fig. 4, however, these two sources are particularly faint in the ALMA data (∼5σ) and have an extended

[5] https://www.eso.org/sci/observing/phase3/data_releases/uvista_dr3.pdf

Table 3. The serendipitous detections found within our ALMA Band 6 data set. The four sources were detected blindly from the data following the procedure outlined in Section 3.2. Column 1 shows the primary target ID of the ALMA pointing in which the source was found. Column 2 is the serendipitous source ID, which is followed by the central coordinates determined from the ALMA data. The measured flux in the ALMA Band 6 imaging is shown in column 5, followed by an estimate of the JH_{140} magnitude obtained using MAG_AUTO from SExtractor in column 6. The offset in the RA and Dec. directions corresponding to the ALMA–*HST* coordinates are shown in columns 7 and 8. In columns 9, we show the photometric or spectroscopic redshift, and finally in column 10, we present the VLA and *Chandra* IDs if available.

PID	ID	RA (J2000)	Dec. (J2000)	$f_{1.3mm}$ (μJy)	JH_{140} (mag)	Δ_{RA}	$\Delta_{Dec.}$	z	Alternative IDs
65666	C1	10:01:39.75	+01:54:56.00	734 ± 58	22.8	−0.02	0.16	$2.00^{+0.13}_{-0.06}$	COSMOSVLADP_J100139.76+015455.8
238225	C2	10:01:51.71	+02:25:46.26	1044 ± 44	22.9	−0.12	−0.04	$1.63^{+0.11}_{-0.06}$	COSMOSVLADP_J100151.72+022546.3
238225	C3	10:01:51.42	+02:25:31.95	476 ± 100	20.1	−0.45	−0.19	0.8268	COSMOSVLADP_J100151.44+022532.1,lid_38
238225	C4	10:01:51.59	+02:25:50.37	272 ± 57	20.3	−0.18	0.03	$0.97^{+0.01}_{-0.01}$	

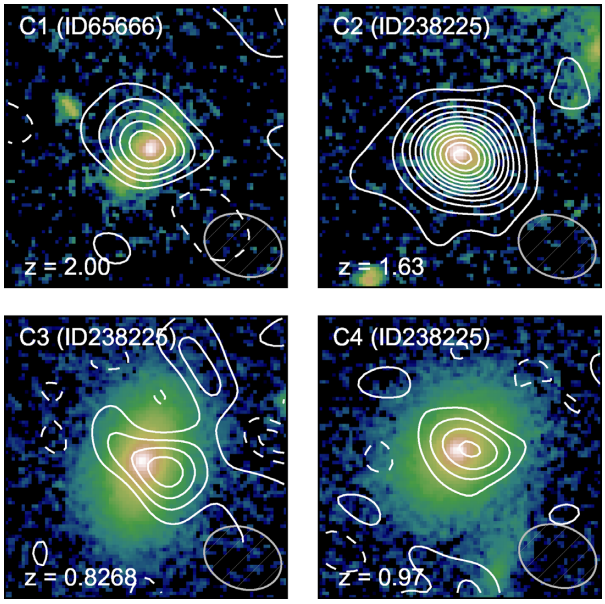

Figure 4. The four serendipitous ALMA sources detected in the pointings for primary target ID65666 (one object) and ID238225 (three objects). The best-fitting photometric redshift, or spectroscopic redshift for object C3, is shown in the lower left of each stamp. Each image is 5 arcsec on a side, with the grey-scale of the background *HST*/WFC3 imaging scaled linearly as in Fig. 1. For the two bright sources (upper row), the ALMA contours are shown in intervals of 2σ.

HST/WFC3 profile. C3 and C4 are also close to the edge of the primary beam, and inspection of the ACS/I_{814} imaging available shows no evidence for colour gradients or obscured components at the observed ALMA position. These factors making the astrometric comparison between the ALMA and *HST*/WFC3 data more uncertain for these galaxies. We therefore focus on the two sources, C1 and C2, when discussing any astrometric systematics. These galaxies are both detected at high SNR by ALMA and are relatively compact in the *HST* data. Visually, these two ALMA bright objects show a good agreement between the peak surface brightness in the *HST*/WFC3 data and the peak in the 1.3 mm profiles. The measured offsets confirm this, with the largest offset being $\Delta_{Dec.} = 0.16$ arcsec for C1 (ID65666). Closer inspection reveals that the JH_{140} profile of this object is asymmetric, which results in the SExtractor centroid being weighted to the south-east of the galaxy (Fig. 4). Note that because these serendipitous sources are at $z \lesssim 2$, the JH_{140} imaging probes the rest-frame wavelengths at > 4000 Å, i.e. the rest-frame optical. We therefore expect the morphology of these sources to be more representative of the underlying stellar mass structure (rather than transient UV star-forming clumps), which traces the most dust obscured regions and hence the location of the expected FIR emission (e.g. Wuyts et al. 2012). We therefore find no evidence for any significant systematic astrometric offset between the ALMA data and near-IR data provided by *HST*/WFC3 and UltraVISTA DR3. This lends weight to the 0.6 arcsec offset observed for the $z \simeq 7$ galaxy ID65666 being a physical separation, rather than an astrometric systematic (see the discussion in Section 5.1).

4 IRX–β RELATION

In order to compare our results to previous studies of the IRX–β relation, we calculate the L_{FIR} for our sample by fitting a modified blackbody assuming a dust temperature of $T = 40$ K (see Section 3). The monochromatic rest-frame UV luminosity is calculated at $\lambda = 1600$ Å as νL_ν, using the measured M_{UV} derived from the JH_{140} data (Bowler et al. 2017). The rest-frame UV slope was measured by fitting a power law to the photometry between $\lambda_{rest} = 1270$–2580 Å (Calzetti, Kinney & Storchi-Bergmann 1994). This corresponds to the *Y*, *J*, and *H* bands at $z \simeq 7$. For the three highest-redshift galaxies we study, there is also the potential contamination of the *Y* band by the Ly α line (if present) or the Lyman break. This is apparent in Fig. A1, where the HSC *y* band, which does not extend as far redwards as the VISTA *Y* band, can be seen to drop in the three galaxies that have $z_{phot} \gtrsim 6.9$. Hence, we additionally exclude the *Y* band in the fitting for ID65666, ID238225, and ID304416. For the stack, we plot the mean β slope of the included galaxies, with the error given by the standard error on the mean. As the results from the full stack and the stack of the non-detections are similar, we show the full stacked results on the IRX–β relation. We calculated the stacked IRX values in two ways: (1) we took the average L_{FIR} determined from the stack, and divided this by the average L_{UV} of the sample and (2) we normalized the ALMA images according to the IRX of each galaxy and then stacked these normalised images to determine the stacked IRX. The results of these two methods were consistent to within $\Delta\log(\mathrm{IRX}) = 0.01$, and hence, we choose to present the results of method (1) here. We show the results from this study on the IRX–β diagram in Fig. 5. On this plot, we also present the Meurer et al. (1999) relation derived at low redshift, assuming both a starburst Calzetti et al. (2000) attenuation law and a steeper SMC extinction law. Both IRX–β relations are plotted assuming an intrinsic rest-frame slope of $\beta = -2.3$ and following the form presented in McLure et al. (2018).

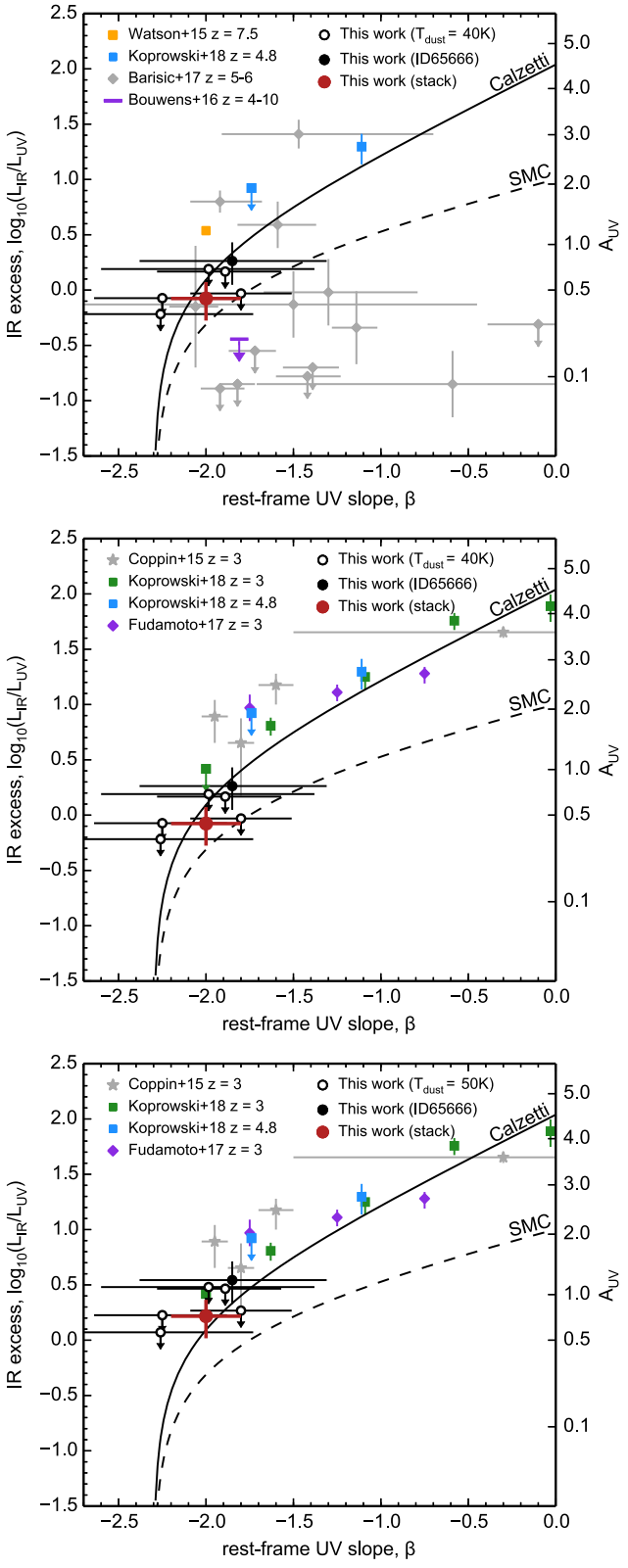

Figure 5. The results of this work on the IRX–β relation. We show the detected galaxy ID65666 (filled circle), the non-detected galaxies (open circles), and the result of stacking the full sample (red circle). Previous studies at $z > 5$ are shown in the upper plot, whereas in the lower plots we compare to studies of $z \simeq 3$–5 LBGs. The final plot shows our results assuming a higher dust temperature of $T = 50$ K. The IRX–β relations are shown assuming the Calzetti (solid line) and SMC dust laws (dashed line).

The only other work that has studied a sample of comparably bright ($L_{\rm UV} > 10^{11}$ L$_\odot$; see Fig. 2) LBGs at $z > 5$ was undertaken by Capak et al. (2015), who selected their sample of 10 $z = 5$–6 galaxies from the ground-based COSMOS field. In Barišić et al. (2017), updated rest-frame UV slopes for the galaxies studied in Capak et al. (2015) were presented, and hence, we compare to this more recent study hereafter. As is evident in the upper panel of Fig. 5, the results from our sample of bright $z \simeq 7$ LBGs occupy a markedly different region of the IRX–β plot than the Barišić et al. (2017) results. Our results do not extend to the extremely low IRX values found by Barišić et al. (2017), which are > 0.5 dex lower than our stack at $z \simeq 7$. Note that if we use an identical parametrization of the FIR SED as Barišić et al. (2017; see Section 3), our derived IRX values would increase by 0.2 dex, further highlighting this discrepancy. We also do not find the large scatter to high IRX values, at a given β, found at $z \simeq 5$. In comparison to the spread of rest-frame UV slopes found by Barišić et al. (2017), we find a tighter range in β in our sample, although the large errors on β in both studies means the majority of the galaxies have formally consistent rest-frame UV slopes. The six LBGs in this study show blue rest-frame UV slopes around $\beta \simeq -2$. This could potentially be due to selection effects (e.g. Dunlop et al. 2013; Rogers, McLure & Dunlop 2013), where redder galaxies are more likely to be classified as contaminant populations (such as dusty $z \simeq 2$ galaxies) and hence be removed from the sample. These objects are very bright, however, being detected up to 2 mag brighter than the limiting magnitudes of the UltraVISTA DR2 data (used for the initial selection), leading to a high completeness as a function of β slope (Bowler et al. 2014). Given the short cosmic time between $z = 7$ and $z = 5$ ($\simeq$400 Myr), it is somewhat surprising that there is such a large difference in these results. The Capak et al. (2015) sample contains both narrow-band selected Ly α emitters (LAEs) and LBGs, which could contribute to the scatter in IRX (e.g. Schaerer et al. 2015); however, Barišić et al. (2017) show that both the LAEs and LBGs with weak or no Ly α emission show similarly low-IRX values. It is possible that using ground-based photometry to measure β, as opposed to higher resolution data from *HST*/WFC3, could bias our measurements to bluer values. This is because we measure β at the peak position of the rest-frame UV emission, which is expected to be the least obscured and hence have the bluest colour (e.g. we measure a 'light-weighted' colour). In the extreme, a dusty star-forming region of a galaxy can become completely obscured in the rest-frame UV, an effect we discuss further in Section 5.1. We cannot measure a resolved β from our current data set, as we only have one *HST*/WFC3 filter (JH_{140}). The comparison of β values derived from the $z \simeq 5$–6 sample of Capak et al. (2015), however, suggest that this effect is not the dominant systematic error on β, as the ground-based measurements in Capak et al. (2015) were found to be redder on the whole, not bluer, than the resolved measurements from *HST*/WFC3 colours presented in Barišić et al. (2017). Note that taking into account the potential offset between the rest-frame UV and FIR emission in ID65666 (Section 5.1) does introduce a larger range in the derived IRX for this object. Ultimately, larger samples of homogeneously selected LBGs with deep ALMA and resolved rest-frame UV imaging will be required to understand these differences.

In Fig. 5, we also compare to the stacked results of Bouwens et al. (2016). Using the ASPECS data in the *Hubble* Ultra Deep Field, Bouwens et al. (2016) found upper limits on the IRX of log(IRX) $\lesssim -0.4$ (2σ; $T = 35$ K) for galaxies at $z = 4$–10. This limit is clearly in tension with the average IRX we find from our stack (and more so with our detection for galaxy ID65666). McLure et al. (2018) have

shown that stacking analyses that use bins of β rather than stellar mass are prone to biases that act to artificially lower the IRX in a given β bin. We therefore only show the full stacked result from Bouwens et al. (2016), rather than the binned results. This point includes galaxies with a wide range in measured rest-frame UV slope, from $\beta \simeq -4$ to $\beta > -1.25$, and hence, the single point should be treated with caution. Furthermore, the majority of the galaxies probed in the ASPECS data were fainter in the rest-frame UV than those studied here, with apparent magnitudes peaking between $m_{\rm AB} = 28$–30 (as opposed to $m_{\rm AB} \simeq 24$–25 for our sample). Nevertheless, the results of this study appear to disagree strongly with the limits obtained from the ASPECS data. Instead (as we discuss below), our results are consistent with the Calzetti-like attenuation law found in lower-redshift galaxies. Similarly, the recent stacking results of Koprowski et al. (2018) at $z = 4.8$ are in good agreement with the Calzetti law, with their study finding no evidence for any evolution in the normalization of the IRX–β relation from $z = 3$–5. Finally, our stacked result is significantly lower than the IRX derived for the lensed galaxy 'A1689-zD1' (Watson et al. 2015) at $z = 7.5$. Whilst the FIR luminosity we determine for our stack is higher than the Watson et al. (2015) and Laporte et al. (2017) objects at $z > 7$, because our sample is more luminous in the UV, the IRX values we derive are lower than these studies. Our results therefore suggest that these two very high-redshift dust detections are not representative of the $z \gtrsim 6$ population as a whole.

Given the small samples sizes and physical differences identified in the previous results at $z > 5$, we also compare our results to previous studies of IRX–β in $z \simeq 3$–5 LBGs. In the middle and bottom panels of Fig. 5, we show the results of Fudamoto et al. (2017), Coppin et al. (2015), and Koprowski et al. (2018), which were all derived from LBGs selected over degree-scale ground-based fields. As such, these $z \sim 3$ samples have a similar UV luminosity and number density to our sample. The results of our study at $z \simeq 7$ are consistent with these previous determinations of IRX–β, overlapping with the blue-end of these data points (e.g. from Koprowski et al. 2018) at the point where the IRX–β relation is predicted to rapidly drop-off. Recent results have indicated that the results at $z \simeq 3$ support a Calzetti-like attenuation curve, with little evidence for a SMC-like extinction law once biases have been corrected for (McLure et al. 2018; Koprowski et al. 2018). In common with these findings, our derived IRX–β points for the individual $z \simeq 7$ LBGs are consistent with a Calzetti-like dust attenuation curve, shown as the solid line in Fig. 5. Whilst there is a large error on the β measurement, the results for galaxy ID65666 are also as expected from the Calzetti law, showing an FIR luminosity that is a factor of 2 brighter than that expected if an SMC-like extinction curve was in effect. With the assumption of a dust temperature of $T = 40$ K, our stacked result is consistent with both a Calzetti and SMC-like dust attenuation/extinction law, with a slightly better agreement with the Calzetti relation. Whilst it has yet to be directly observed in $z > 5$ LBGs, several observational works have suggested that the dust temperature at these redshifts could be substantially higher (e.g. Béthermin et al. 2014; Schreiber et al. 2017). Indeed, some theoretical models/simulations indicate the dust temperature could be as high as $\simeq$60 K at $z = 7$ (Imara et al. 2018; Narayanan et al. 2018), with potential variations in T between individual galaxies in the same sample (Pavesi et al. 2016). We therefore also present the derived IRX–β results for our sample assuming a higher dust temperature of $T = 50$ K in the bottom panel of Fig. 5. The result is a vertical shift of 0.3 dex due to the derived $L_{\rm FIR}$ being double that obtained assuming our fiducial dust temperature. Clearly in the case of an evolving dust temperature, our results are in excellent agreement with the $z \simeq 3$ Calzetti-like relation. In this case, our stacked results exclude an SMC-like extinction law at the $\gtrsim 2\sigma$ level. In conclusion, we find no compelling evidence for extremely low IRX values at $z > 5$ as has previously been claimed by Capak et al. (2015) and Bouwens et al. (2016) from our sample of UV bright LBGs at $z \simeq 7$. Instead, particularly if the dust temperature is evolving with redshift, our results are fully consistent with a Calzettti-like dust attenuation curve as found in local starburst galaxies.

5 DISCUSSION

5.1 A physical offset between the UV and FIR emission

When comparing the *HST*/WFC3 JH_{140} band image to the ALMA 1.3 mm detection in object ID65666, we find an offset of 0.6 arcsec predominantly in the north–south direction ($\Delta_{\rm RA} = 0.57$ arcsec, $\Delta_{\rm Dec.} = 0.17$ arcsec). Offsets between the dust continuum and rest-UV emission have been identified in several high-redshift LBGs (Koprowski et al. 2016; Faisst et al. 2017; Laporte et al. 2017), as have offsets between the [C II] FIR line and the rest-UV continuum (e.g. Capak et al. 2015; Maiolino et al. 2015; Willott et al. 2015; Carniani et al. 2017). Some of these offsets have been attributed to astrometric systematics (e.g. Dunlop et al. 2017), however, there is a growing consensus that FIR emission lines in particular are physically offset at $z \simeq 7$ (see Carniani et al. 2018). The offset we observe corresponds to a physical separation of $\simeq$3 kpc. This separation is comparable in magnitude to what has been found previously in high-redshift LBGs (e.g. in HZ4 and HZ10; Faisst et al. 2017). The physical nature of this offset is strengthened by the presence of a bright ALMA source in the same primary beam as ID65666 (Fig. 4), which shows no significant astrometric offset (see Section 3.2). The expected positional accuracy in the ALMA data is given as $0.6 \times$ FWHM/SNR (Ivison et al. 2007), which corresponds to $\sigma = 0.17$ along the major axis and $\sigma = 0.13$ along the minor axis of the beam. We therefore find that the offset has a significance of $\simeq 4\sigma$ in the absence of systematic errors (which our checks have demonstrated are minimal). Note that in Carniani et al. (2018) they shift the near-IR data such that serendipitous sources are perfectly aligned with the ALMA data. In this case, the observed astrometric offset observed for ID65555 would be 0.45 arcsec, which is still a $\sim 3\sigma$ separation.

As shown in the enlarged image in Fig. 6, the rest-frame UV emission for ID65666 shows a clumpy, extended morphology. In comparison to the ALMA contours, the observed rest-frame UV emission appears to wrap around the central obscured part, as is seen in dusty star-forming galaxies and submillimetre galaxies at low redshift (e.g. Hodge et al. 2015; Chen et al. 2017). In the prediction of a relationship between the IRX and the rest-frame UV slope, there is the assumption that the stars and dust are well mixed, leading to the coupling of any observed reddening in the UV to the FIR emission detected (e.g. Charlot & Fall 2000). If instead, the galaxy consists of regions of significantly different obscuration, then the relationship will break down for the galaxy as a whole. At the central position of the 1.3 mm detection for ID65666, we find no evidence for rest-frame UV emission in the *HST*/WFC3 data. The 'UV-dark' part of this LBG therefore has a high IRX (and potentially very red β), which is significantly different to the value derived for the full galaxy. Taking the 2σ upper limit of the JH_{140} data as $m_{\rm AB} = 27.9$ (equivalent to $M_{\rm UV} \lesssim -19$), we estimate that the IRX of this obscured region is IRX $\gtrsim 1.5$ corresponding to an $A_{\rm UV} \simeq 3$ mag. Conversely, for the UV-visible part of the LBG found within the *HST* data, the IRX value is lower than that calculated for

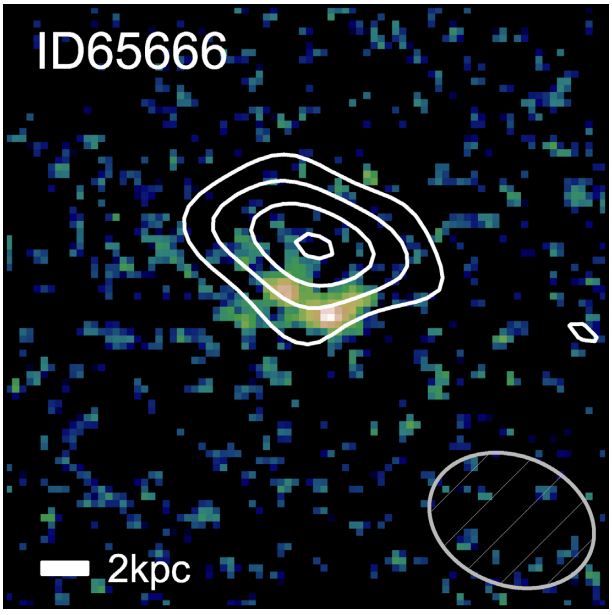

Figure 6. The FIR detected galaxy, ID65666, at $z = 7.17^{+0.09}_{-0.06}$. The background image shows the *HST*/WFC3 JH_{140} data probing the rest-frame UV emission. The ALMA Band 6 data probing the rest-frame FIR dust continuum is shown as the contours, which are displayed upwards and including 2σ significance. An offset of 0.6 arcsec is seen between the datasets, corresponding to a physical separation of 3 kpc (see Sections 3.2 and 5.1 for discussion). The image is 5 arcsec on the side, and the beam is shown as the grey ellipse in the lower right-hand corner.

the full object if the dust emission is physically decoupled. If we assume that there is no 1.3 mm emission at the 2σ level from the UV-bright part of the LBG, this results in an upper limit on the IRX $< -0.35\,(2\sigma)$, which is still consistent with what would be expected the IRX–β relation found at lower redshift (given the errors on β). Thus within ID65666, we find a considerable range in the measured IRX across the galaxy (see also Koprowski et al. 2016 and the discussion in Faisst et al. 2017), and evidence that the observed rest-UV emission is spatially distinct from the site of strong dust emission. Such a decoupling of the galaxy colour and FIR emission has been observed in IR-selected galaxies, where above $L_{\rm FIR} > 10^{11}\,{\rm L}_{\odot}$ galaxies appear bluer than expected from the IRX–β relation (Casey et al. 2014b).

In our stacking analysis, we find evidence that the FIR flux is extended when stacking is performed based on the rest-frame UV position. If offsets between the rest-UV and rest-FIR emission like that observed for ID65666 are common in our sample, then this would provide a natural explanation for the extended flux observed in the stack (Fig. 3). If spatial offsets of the order of ∼0.5 arcsec are common within the LBG population (as they are in the SMG population; Riechers et al. 2014; Chen et al. 2017), this could result in a reduced sensitivity to flux when stacking based on the rest-frame UV position. To test this hypothesis, we performed a simple simulation of stacking artificial ALMA sources with spatial offsets in random directions. We assumed a Gaussian profile with a FWHM of 1 arcsec, to approximate the ALMA beam in our observations. In the case of a constant 0.5 arcsec offset, we find that the SNR was approximately half that expected if the rest-frame UV and FIR centroid were the same (assuming naturally weighted images). In the case of a distribution of offsets, chosen randomly between 0 and 0.5 arcsec, the stacked flux was only marginally lower than with no assumed offset. Clearly, the result depends sensitively on the resolution of the FIR data sets (such that SCUBA-2 stacking, for example, would be unaffected), on the magnitude of the offset, and on the method used to measure the flux. We therefore conclude that such an effect is unlikely to be important for the fainter LBG population at high redshift, which tend to show compact and smooth profiles (Curtis-Lake et al. 2016), but could be significant for bright galaxies where the observed dust and UV emission are extended on the scale of ≃1 arcsec.

5.2 The star formation rate and $M_\star$ of bright LBGs at $z = 7$

We calculated the FIR star formation rate using the calibration from Kennicutt & Evans (2012), correcting to a Chabrier (2003) IMF. The SFR from the observed (uncorrected) rest-frame UV emission was estimated using the Madau, Pozzetti & Dickinson (1998) prescription corrected to a Chabrier (2003) IMF. The UV SFR was found to be in the range of 17–34 $\rm M_{\odot}\,yr^{-1}$ for the sample (Bowler et al. 2017). For the stack, we find that the obscured SFR ($\rm SFR_{FIR}$ ≃ $30\,\rm M_{\odot}\,yr^{-1}$) is comparable to that observed in the rest-frame UV. Clearly, therefore, dust obscured star formation is significant in bright $z \simeq 7$ LBGs. Furthermore, if the dust temperature is higher at these redshifts than our fiducial value, then the $\rm SFR_{FIR}$ would be even higher (by a factor of 2 for $T = 50$ K). In the individually detected galaxy ID65666, the obscured component of the SFR is even larger, with 75 per cent of the total SFR being obscured (increasing to 85 per cent in the case of $T = 50$ K).

In comparison to the full sample, our FIR-detected object ID65666 appears unremarkable in terms of $\rm SFR_{UV}$ and rest-frame UV slope. In fact, it has one of the lower SFRs as derived from the observed magnitude in the rest-frame UV. Recent results at z ≃ 3 have highlighted the importance of stellar mass in predicting the dust attenuation, or IRX, of star-forming galaxies (Bourne et al. 2017; Dunlop et al. 2017; McLure et al. 2018). We therefore estimated the stellar masses of the galaxies in our sample, with the expectation that ID65666 would be one of the most massive. We performed SED fitting to the available optical, near-, and mid-IR data. Crucially, this includes *Spitzer*/IRAC photometry that probes the rest-frame optical emission at $z \simeq 7$. At these redshift, however, strong rest-frame optical emission lines of H α, H β, and [O III] can contaminate the [3.6] and [4.5] bands and artificially boost the derived masses. The SED fits are shown in Fig. A1 and the derived stellar masses in Table 2. We find evidence for strong rest-frame optical emission lines in our sample (Bowler et al. 2017). To provide estimates of the masses, we therefore excluded bands that were potentially contaminated based on the galaxy redshift. For the lowest-redshift galaxy in our sample, ID279127, potentially both of the *Spitzer*/IRAC [3.6] and [4.5] bands contain strong emission lines. For this galaxy, we fit to the [4.5] band only, which contains H α at $z \lesssim 6.6$, and caution that in this case the stellar mass represents an upper limit. The stellar masses of our sample are found to be $\log(M_\star/\rm M_{\odot}) \simeq 9.5$. In comparison to the IRX–$M_\star$ relation, our sample lies below the relation derived at $z \simeq 2$ by McLure et al. (2018) as has been found for other high-redshift samples (Faisst et al. 2017; Fudamoto et al. 2017). The tension would be reduced if the dust temperature is higher at these redshifts, and considering the large errors present in the determination of stellar masses at these redshifts, we cannot make strong conclusions in this study about the presence of an IRX–$M_\star$ relation at $z \simeq 7$.

Galaxy ID65666 shows a particularly low mass of $\log(M_\star/\rm M_{\odot}) = 9.0^{+0.8}_{-0.2}$ (although the error is large due to the low-significance detection in the [3.6] band) and also shows the reddest

[3.6]–[4.5] colour, indicative of particularly strong rest-frame optical emission lines. Note that the mass we measure is determined from the unobscured part of the LBG, hence could be underestimated. Using the flux excess in the [3.6] band compared to the best-fitting continuum model, we estimate that the rest-frame equivalent width of the combined H β + [O III] lines is $EW_0 = 1400 \pm 300$ Å for this galaxy (uncorrected for dust attenuation), making it comparable to some of the most extreme nebular emitters known at these redshifts (Roberts-Borsani et al. 2015; Bowler et al. 2017). The properties of ID65666 suggest that it is a dusty starburst, showing an anisotropic distribution of unobscured and obscured star formation on the scale of several kpc. As such it has a similar morphology and properties (although with weaker dust emission by a factor of 100) as has been observed for high-redshift submillimetre galaxies (e.g. Casey et al. 2014a; Hodge et al. 2015; Chen et al. 2017).

5.3 Dust in galaxy formation simulations at high redshifts

In Bowler et al. (2015), we presented a comparison between the observed rest-frame UV LF at $z = 5$–7 and that predicted by a range of cosmological galaxy formation simulations. One notable trend was that the majority of these simulations over predicted the number density of LBGs brightwards of $M_{UV} \lesssim -20$. This excess of galaxies at the bright end is present in hydrodynamical simulations (e.g. Illustris, Genel et al. 2014; FIRE, Ma et al. 2018; and the FiBY model; Cullen et al. 2017), semi-analytic models (e.g. the Munich L-galaxies model, Clay et al. 2015; GALFORM, Gonzalez-Perez et al. 2013; and the Somerville et al. 2012 model), as well as the analytic model of Cai et al. (2014). Within these simulations, the observed number densities were only reproduced with the addition of a considerable amount of dust, which acts to suppress the rest-frame UV emission. For example, in the Munich model presented in Clay et al. (2015), galaxies with an observed $M_{UV} < -22$ are predicted to have a UV attenuation of $A_{UV} \simeq 2$ mag. In the case of a uniform distribution of dust covering the star-forming regions, such an attenuation would result in red rest-frame UV colours of $\beta \gtrsim -1.5$ depending on the dust attenuation law assumed. At $z \simeq 5$, Cullen et al. (2017) have shown using the FiBY model that such an attenuation is consistent with the observed colour–magnitude relationship, with the brightest UV galaxies being attenuated more and showing redder colours.

In the case of well-mixed stars and dust, the IRX is directly related to the attenuation in the UV, whereas the relationship between IRX and β depends on the dust attenuation law. It is therefore possible to directly test the expected attenuation using the measurements of the FIR dust continuum for our sample. We show the A_{UV} on the right-hand y-axis of Fig. 5. The measured FIR emission from our sample implies an average UV attenuation of $A_{UV} \simeq 0.5$–1.0 mag (depending on dust temperature). Our results therefore show that the presence of dust is significant in suppressing the observed UV luminosity in the brightest galaxies. Whilst the average magnitude of the attenuation is lower than that predicted in some of the models described above, it is sufficient to have a significant effect on the observed number counts of UV bright LBGs observed at these redshifts. Moreover, the detection of completely obscured star formation in galaxy ID65666 in this work highlights the possibility that some star-forming galaxies may be completely obscured in the rest-frame UV, even at redshifts as high as $z = 7$. If this is the case, then optical/near-IR surveys for high-redshift LBGs will form an incomplete census of star formation. Our results indicate that a combination of dust obscuring around 50–85 per cent of the star formation in bright LBGs, plus the presence of 'UV-dark' galaxies that are missing from current UV selected samples, can explain the observed shape of the bright-end of the rest-frame UV LF at $z \simeq 7$.

6 CONCLUSIONS

We present new ALMA imaging at 1.3 mm (rest frame $\simeq$170 μm) of six bright LBGs at $z \simeq 7$. The sample was originally selected from 1 deg^2 of the COSMOS field, and represents some of the most intrinsically UV luminous galaxies at this epoch ($M_{UV} < -22$). We observe the sample with 10 min integrations in ALMA Band 6. The highest redshift galaxy targeted, ID65666 at $z = 7.17^{+0.09}_{-0.06}$, is detected at 5σ significance at peak emission, corresponding to a FIR luminosity of $L_{FIR} \simeq 3.6 \pm 1.2 \times 10^{11}$ L$_\odot$. The five remaining galaxies are undetected at the 3σ level. The average FIR luminosity of the sample, determined from a stacking analysis, is $L_{FIR} \simeq 2 \times 10^{11}$ L$_\odot$. Converting this observed L_{FIR} into a SFR indicates that in these galaxies, approximately half of the total SFR is obscured by dust. In comparison to the IRX–β relation, we do not reproduce the extremely low-IRX values found at $z > 5$ by several previous studies (Capak et al. 2015; Bouwens et al. 2016). Instead, our results are consistent with the predictions of the Calzetti-like dust attenuation law found for star-forming galaxies at lower redshifts. We find that the presence of dust in the brightest LBGs is significant in shaping the observed UV LF at the bright end, with galaxies of absolute magnitude $M_{UV} < -22$ being attenuated by $A_{UV} = 0.5$–1.0 on average. Such an attenuation is comparable to that typically applied in galaxy formation simulations. In the galaxy ID65666 at $z = 7.17^{+0.09}_{-0.06}$, we detect a physical offset between the rest-frame FIR dust continuum probed by ALMA and the rest-frame UV emission probed by *HST*/WFC3 JH_{140} imaging. The offset is measured to be 0.6 arcsec, corresponding to a physical separation of 3 kpc. The detection of a serendipitous source in the same ALMA pointing rules out any significant astrometric systematic. The presence of this offset indicates an inhomogeneous distribution of dust within this galaxy, with a high proportion of the total SFR (>75 per cent) being completely obscured in the rest-frame UV. The existence of this obscured component in galaxy ID65666 illustrates that entire star-forming regions, or potentially even entire galaxies, could be 'UV dark' even at $z \simeq 7$.

ACKNOWLEDGEMENTS

Korea Astronomy and Space Science InstituteMinistry Of Science and TechnologyNational Research CouncilNational Institutes of Natural SciencesNational Science FoundationThis work was supported by the Oxford Hintze Centre for Astrophysical Surveys that is funded through generous support from the Hintze Family Charitable Foundation. NB acknowledges support from the European Research Council Advanced Investigator Program, COSMICISM (ERC-2012-ADG_20120216, PI: R. J. Ivison). This paper makes use of the following ALMA data: ADS/JAO.ALMA#2015.1.00540.S. ALMA is a partnership of the European Southern Observatory (ESO; representing its member states), (USA), and (Japan), together with (Canada), and Academia Sinica Institute of Astronomy and Astrophysics (Taiwan), and (Republic of Korea), in cooperation with the Republic of Chile. The Joint ALMA Observatory is operated by ESO, Associated Universities, Inc./National Radio Astronomy Observatory and National Astronomical Observatories of Japan. This work is based in part on observations made with the NASA/European Space Agency *HST*, which is operated by the Association of Universities for Research in Astronomy, Inc., under NASA contract NAS5-26555. This research made use of ASTROPY,

a community-developed core PYTHON package for Astronomy (Astropy Collaboration 2013).

REFERENCES

Aihara H. et al., 2017, PASJ, 70, S8
Álvarez-Márquez J. et al., 2016, A&A, 587, A122
Arnouts S., Cristiani S., Moscardini L., Matarrese S., Lucchin F., Fontana A., Giallongo E., 1999, MNRAS, 310, 540
Ashby M. L. N. et al., 2018, ApJS, 237, 39
Astropy Collaboration, 2013, A&A, 558, A33
Barišić I. et al., 2017, ApJ, 845, 41
Bertin E., 2011, in Evans I. N., Accomazzi A., Mink D. J., Rots A. H., eds, ASP Conf. Ser. Vol. 442, Astronomical Data Analysis Software and Systems XX. Astron. Soc. Pac., San Francisco, p. 435
Bertin E., Arnouts S., 1996, A&AS, 117, 393
Bertoldi F., Carilli C. L., Cox P., Fan X., Strauss M. A., Beelen A., Omont A., Zylka R., 2003, A&A, 406, L55
Béthermin M. et al., 2014, A&A, 573, A113
Bourne N. et al., 2017, MNRAS, 467, 1360
Bouwens R. J. et al., 2011, Nature, 469, 504
Bouwens R. J. et al., 2014, ApJ, 793, 115
Bouwens R. J. et al., 2016, ApJ, 833, 72
Bowler R. A. A. et al., 2012, MNRAS, 426, 2772
Bowler R. A. A. et al., 2014, MNRAS, 440, 2810
Bowler R. A. A. et al., 2015, MNRAS, 452, 1817
Bowler R. A. A., Dunlop J. S., McLure R. J., McLeod D. J., 2017, MNRAS, 466, 3612
Bruzual G., Charlot S., 2003, MNRAS, 344, 1000
Cai Z.-Y., Lapi A., Bressan A., De Zotti G., Negrello M., Danese L., 2014, ApJ, 785, 65
Calzetti D., Kinney A. L., Storchi-Bergmann T., 1994, ApJ, 429, 582
Calzetti D., Armus L., Bohlin R. C., Kinney A. L., Koornneef J., Storchi-Bergmann T., 2000, ApJ, 533, 682
Capak P. L. et al., 2015, Nature, 522, 455
Carniani S. et al., 2017, A&A, 605, A42
Carniani S. et al., 2018, MNRAS, 1184, 1170
Casey C. M., 2012, MNRAS, 425, 3094
Casey C. M., Narayanan D., Cooray A., 2014a, Phys. Rep., 541, 45
Casey C. M. et al., 2014b, ApJ, 796, 95
Chabrier G., 2003, PASP, 115, 763
Charlot S., Fall S. M., 2000, ApJ, 539, 718
Chen C.-c., Hodge J. A., Smail I., Swinbank A. M., Walter F., Simpson J. M., 2017, ApJ, 846, 108
Civano F. et al., 2016, ApJ, 819, 62
Clay S., Thomas P., Wilkins S., Henriques B., 2015, MNRAS, 415, 2692
Coppin K. E. K. et al., 2015, MNRAS, 446, 1293
Cullen F., McLure R. J., Khochfar S., Dunlop J. S., Vecchia C. D., 2017, MNRAS, 470, 3006
Curtis-Lake E. et al., 2016, MNRAS, 457, 440
da Cunha E. et al., 2013, ApJ, 766, 13
Dunlop J. S. et al., 2013, MNRAS, 432, 3520
Dunlop J. S. et al., 2017, MNRAS, 466, 861
Faisst A. L. et al., 2017, ApJ, 847, 28
Fudamoto Y. et al., 2017, MNRAS, 472, 483
Furusawa H. et al., 2016, ApJ, 822, 46
Genel S. et al., 2014, MNRAS, 445, 175
Gonzalez-Perez V., Lacey C. G., Baugh C. M., Frenk C. S., Wilkins S. M., 2013, MNRAS, 429, 1609
Hashimoto T. et al., 2018, preprint (arXiv:1806.00486)
Henriques B., White S., Thomas P., Angulo R., Guo Q., Lemson G., Springel V., Overzier R., 2015, MNRAS, 451, 2663
Hodge J. A., Riechers D., Decarli R., Walter F., Carilli C. L., Daddi E., Dannerbauer H., 2015, ApJ, 798, L18
Ilbert O. et al., 2006, A&A, 457, 841
Imara N., Loeb A., Johnson B. D., Conroy C., Behroozi P., 2018, ApJ, 854, 36
Indebetouw R. et al., 2014, ApJ, 782, L2
Ivison R. J. et al., 2007, MNRAS, 380, 199
Kennicutt R. C., Evans N. J., 2012, ARA&A, 50, 531
Knudsen K. K., Watson D., Frayer D., Christensen L., Gallazzi A., Michalowski M. J., Richard J., Zavala J., 2017, MNRAS, 466, 138
Koekemoer A. M. et al., 2007, ApJS, 172, 196
Koprowski M. P. et al., 2016, MNRAS, 828, L21
Koprowski M. P. et al., 2018, MNRAS, 479, 4355
Laigle C. et al., 2016, ApJS, 224, 24
Laporte N. et al., 2017, ApJ, 837, L21
Lilly S. J. et al., 2007, ApJS, 172, 70
Ma X. et al., 2018, MNRAS, 478, 1694
Madau P., Pozzetti L., Dickinson M., 1998, ApJ, 498, 106
Magnier E. A. et al., 2016, preprint (arXiv:1612.05242)
Maiolino R. et al., 2015, MNRAS, 452, 54
Massey R., Stoughton C., Leauthaud A., Rhodes J., Koekemoer A., Ellis R., Shaghoulian E., 2010, MNRAS, 401, 371
McCracken H. J. et al., 2012, A&A, 544, A156
McLeod D. J., McLure R. J., Dunlop J. S., 2016, MNRAS, 459, 3812
McLure R. J. et al., 2018, MNRAS, 476, 3991
Meurer G. R., Heckman T. M., Calzetti D., 1999, ApJ, 521, 64
Michałowski M. J., 2015, A&A, 577, A80
Michałowski M. J., Murphy E. J., Hjorth J., Watson D., Gall C., Dunlop J. S., 2010, A&A, 522, A15
Narayanan D., Dave R., Johnson B., Thompson R., Conroy C., Geach J. E., 2018, MNRAS, 474, 1718
Oke J. B., 1974, ApJS, 27, 21
Oke J. B., Gunn J. E., 1983, ApJ, 266, 713
Ouchi M. et al., 2010, ApJ, 723, 869
Pavesi R. et al., 2016, ApJ, 832
Peng Y. et al., 2010, ApJ, 721, 193
Pope A. et al., 2008, ApJ, 675, 1171
Popping G., Somerville R. S., Galametz M., 2017, MNRAS, 471, 3152
Reddy N. A. et al., 2017, ApJ, 853, 56
Riechers D. A. et al., 2013, Nature, 496, 329
Riechers D. A. et al., 2014, ApJ, 796, 84
Roberts-Borsani G. W. et al., 2015, ApJ, 823, 143
Rogers A. B., McLure R. J., Dunlop J. S., 2013, MNRAS, 429, 2456
Rogers A. B. et al., 2014, MNRAS, 440, 3714
Schaerer D., Boone F., Zamojski M., Staguhn J., Dessauges-Zavadsky M., Finkelstein S., Combes F., Richard J., 2015, A&A, 574, 10
Schreiber C., Elbaz D., Pannella M., Ciesla L., Wang T., Franco M., 2017, A&A, 609, A30
Scoville N. et al., 2007a, ApJS, 172, 1
Scoville N. et al., 2007b, ApJS, 172, 38
Somerville R. S., Gilmore R. C., Primack J. R., Domínguez A., 2012, MNRAS, 423, 1992
Steinhardt C. L. et al., 2014, ApJ, 791, L25
Todini P., Ferrara A., 2001, MNRAS, 325, 726
Valiante R., Schneider R., Bianchi S., Andersen A. C., 2009, MNRAS, 397, 1661
Wang R. et al., 2007, ApJ, 134, 617
Watson D., Christensen L., Knudsen K. K., Richard J., Gallazzi A., Michałowski M. J., 2015, Nature, 519, 327
Willott C. J., Carilli C. L., Wagg J., Wang R., 2015, ApJ, 807, 9
Wuyts S. et al., 2012, ApJ, 753, 114

APPENDIX A: SED-FITTING RESULTS

In Fig. A1, we show the results of our SED-fitting analysis to determine the best-fitting photometric redshifts and to provide an estimate of the stellar masses. We fit to 16 bands, which consist of the CFHT *u*∗*gri* bands, the Subaru/HSC *GRIZy* bands, the deeper Subaru/SuprimeCam z'-band data (Furusawa et al. 2016), the VISTA *YJHK*$_s$ bands from UltraVISTA DR3, and finally the available *Spitzer*/IRAC [3.6] and [4.5] data. The inclusion of the HSC *y*-band data in particular results in more precise photomet-

ric redshifts for our sample as compared to our previous analyses (Bowler et al. 2014, 2017), as it probes close to the Lyman-break at $z \simeq 7$, but does not extend as far to the red as the VISTA *Y*-band filter. In Fig. A1, we also show the resulting χ^2 distribution as a function of redshift. Despite the inclusion of low-redshift contaminant SED models in the fitting procedure (e.g. old and dusty templates, with up to $A_V = 6$), none of the galaxies show an acceptable fit at $z < 6.5$, demonstrating the robustness of the high-redshift solution. We excluded the *HST*/WFC3 JH_{140} photometry from the fitting. Whilst these data are nominally deeper than the ground-based imaging, because the galaxies considered in this study are highly extended, large apertures are required to capture the total flux. The result is that including the JH_{140} data provides minimal additional constraints on the SED over the narrower ground-based filters (although both data sets are consistent; Bowler et al. 2017).

APPENDIX B: INVESTIGATING POTENTIAL BIASES IN THE MEASUREMENT OF THE REST-FRAME UV SLOPE

We investigated the robustness of our measurement of β using injection and recovery simulations. Simulated galaxies were created assuming an underlying Sersic profile with a Sersic index of $n = 1.5$ and a half-light radius of $r_{1/2} = 2.0$ kpc. These parameters were chosen to match those found from stacking the *HST*/WFC3 imaging for the brightest (and most extended) galaxies at $z \simeq 7$ (Bowler et al. 2017), including the objects in this sample. We injected these fake sources with apparent magnitudes in the range [21, 26], and with β values in the range $[-3.0, 0.0]$. To account for the varying depth across the UltraVISTA near-IR imaging, simulations were performed in subsets of the data (7 arcmin on a side) around each high-redshift candidate. The simulations exactly reproduced the source extraction and β measurements followed for the real objects. Multiple runs were produced to ensure minimal overlap or overcrowding between simulated sources, which were placed in random blank positions in the image. Blank positions were determined using the segmentation map produced by SExtractor. In Fig. B1, we show the results of these simulations for an input $\beta = -2.0$. Approximately 1500 recovered sources are shown. We find no significant bias in the recovery of the rest-frame UV slope from the UltraVISTA data, both when fitting to the *Y*, *J*, and *H* photometry, and also when fitting to the *J* and *H* photometry alone (as is the case for ID65666). We find a larger scatter when only fitting to the *J* and *H* bands as expected, however, for object ID65666 it is necessary to remove the *Y* band from the fitting due to the Lyman-break falling in this band. Finally, the scatter we find agrees well with the derived errors in β, providing reassurance that these error bars are realistic.

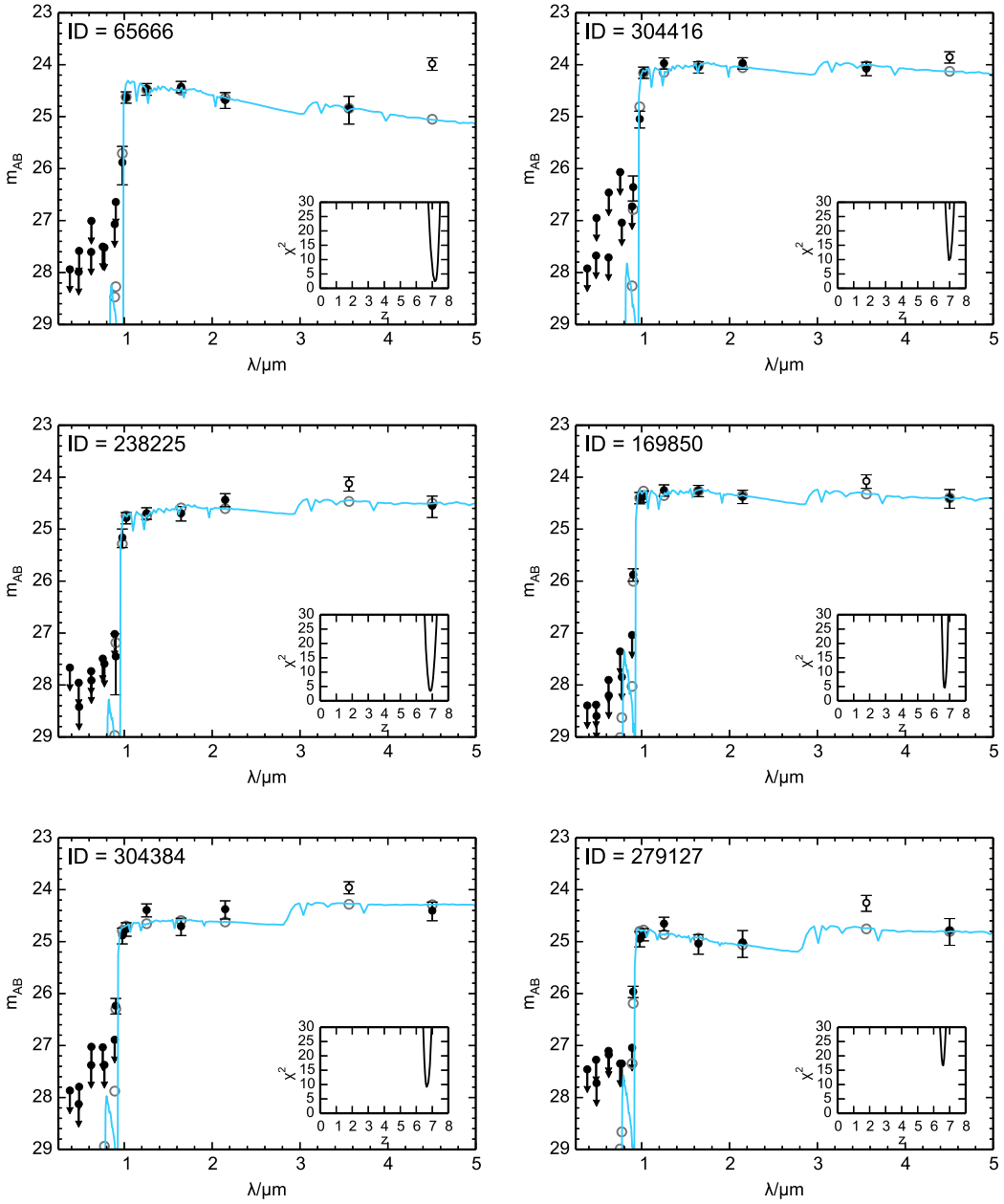

Figure A1. The optical, near and mid-IR photometry for the six galaxies targeted with ALMA. The best-fitting SED model is shown as the blue line. We excluded either the [3.6] or [4.5] bands in the fitting due to contamination by rest-frame optical emission lines. Excluded bands are shown as the open data points. The grey open circles show the expected magnitude in that band derived from the best-fitting model. The inset plot shows the χ^2 as a function of redshift derived from our SED-fitting analysis.

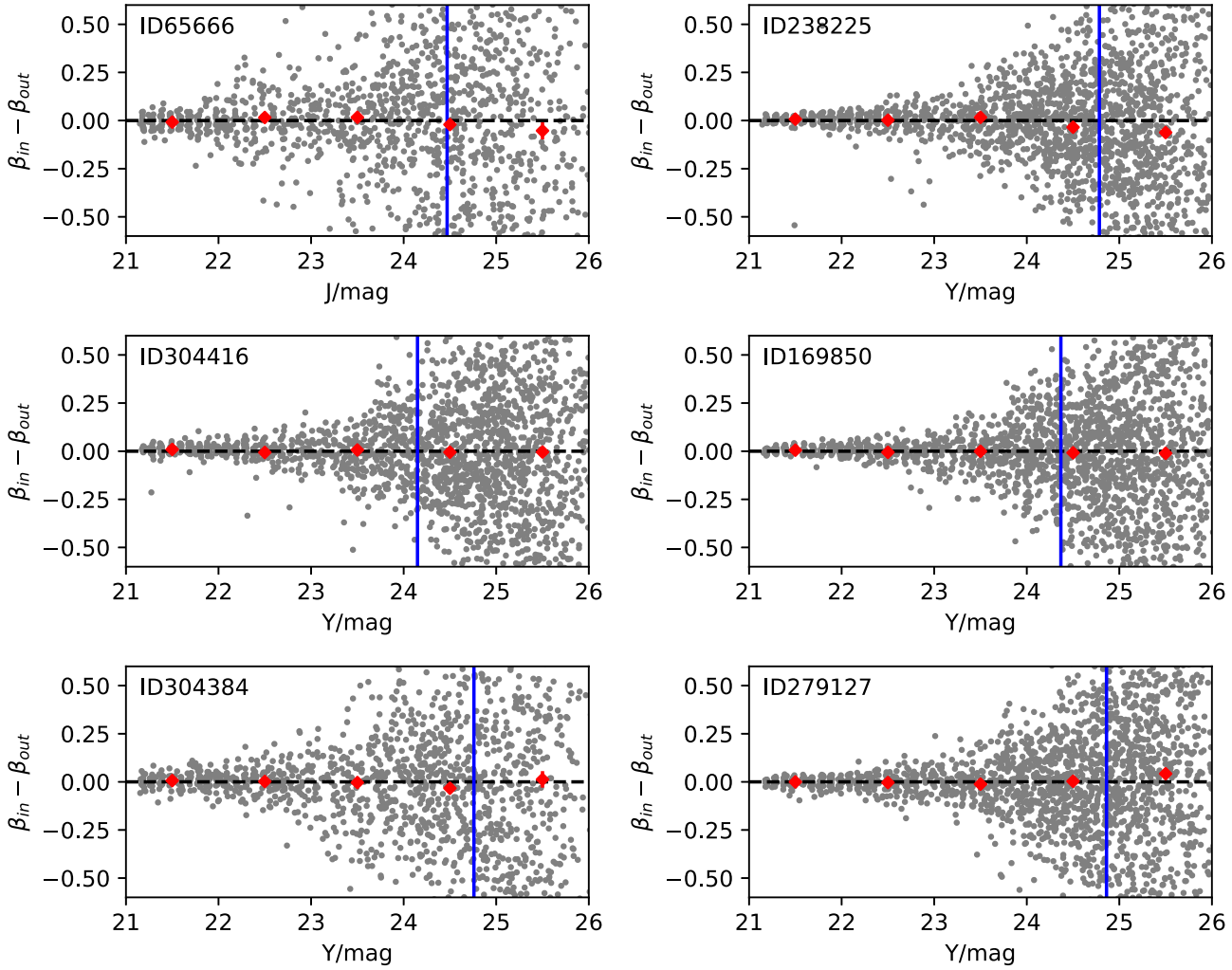

Figure B1. The results of injection and recovery simulations with an input of $\beta = -2.0$. The difference between the input and measured β is plotted against the output total magnitude in either the Y or J band. Results for individual injected sources are shown as the grey points, with the mean and standard error on the mean shown as the red diamonds for bins in magnitude ($\Delta m = 1.0$). Each panel shows the results of the simulations performed in the region of data surrounding each of our six sources. For ID65666, the results are derived by fitting to the J and H bands only, for the remaining sources the Y, J, and H are included in the power-law fit to derive β. The vertical blue line in each plot shows the observed total magnitude of the object. A black dashed horizontal line is shown at $\beta_{\rm in} - \beta_{\rm out} = 0.0$ to guide the eye.

This paper has been typeset from a TEX/LATEX file prepared by the author.